Article

Acceptor engineering of quinone-based cycloparaphenylenes via post-synthesis for achieving white-light emission in single-molecule

Xiaonan Li, Lin Liu, Luyang Jia, Zhe Lian, Jing He, Shengzhu Guo, Ying Wang ⓘ ✉, Xuebo Chen ⓘ ✉ & Hua Jiang ⓘ ✉

Developing donor-acceptor [n]cycloparaphenylenes (D-A [n]CPPs) with multiple emissions from different emissive states remains challenging yet crucial for achieving white-light emission in single-molecule. Here, we report our explorations into acceptor engineering of quinone-based D-A [10]CPPs (**Nq/Aq/Tq[10]CPPs**) via a post-lateral annulation using Diels-Alder reactions of **oxTh[10]CPP**. X-ray analysis reveals that **Nq[10]CPP** displays a side by side packing via naphthoquione stacking while **Aq[10]CPP** adopts an intercalated conformation through anthraquinone interaction. Fluorescence investigations reveal that the quinone-based [10]CPPs display distinctive acceptor-dependent dual-emission from both the locally excited state and charge transfer state after single-wavelength excitation in organic solvents, consequently leading to multicolor emissions, in particular, white-light emission in $CHCl_3$ for **Aq[10]CPP**. In THF/water mixture, quinone-based [10]CPPs and **oxTh[10]CPP** display a wide range of fluorescence emissions including white-light emission as increasing the fraction of water, accompanying by the formation of nanoparticles as demonstrated by Tyndall effect and SEM. Interestingly, the fluorescence of **Aq[10]CPP** can be switched from white to blue in $CHCl_3$ upon redox. Our investigations demonstrate that acceptor engineering not only endows quinone-based [10]CPPs with two distint emissive states for achieving white-light emission but also highlights an effective post-synthetic strategy for functionalizing CPP nanohoops with desirable properties.

Extensive investigations on [n]cycloparaphenylenes have uncovered their distinct size-dependent photophysical properties due to their unique in-plane radial conjugated structure[1–5], and ultimately established [n]CPPs as a remarkably versatile platform that can be tailored for diverse applications, such as chiral recognition[6], mechanically interlocked molecules[7–18], hierarchical self-assembly[19–21], organic electronic devices[22–32], fluorescence imaging[33,34], circularly polarized luminescene[35–40] and beyond[2,41–50]. The incorporation of an electron

donor (D) or acceptor (A) into the framework of [n]CPPs typically results into a significant separation of the frontier molecular orbitals, which leads to a narrower optical band gap, and in turn, enables effective modulation of the electrochemical and photoelectric properties of [n]CPPs[51]. The bending of the π-system in CPPs also leads to an elevation of its highest occupied molecular orbital energy (HOMO) compared to that of its linear counterparts, thereby establishing their electron-donating characteristics. Thus, the integration of electron

College of Chemistry, Beijing Normal University, Beijing 100875, P.R. China. ✉e-mail: ywang1@bnu.edu.cn; xuebochen@bnu.edu.cn; jiangh@bnu.edu.cn

acceptors into the electron donor CPP nanohoop holds significant implications for advancing the development of CPPs in material science[4,52–55] and supramolecular chemistry[42,56]. In this context, only a few elegant examples on D-A CPPs were reported[57–63] (Fig. 1a). In these reported D-A CPPs, the acceptors were fully embedded into the CPP backbone, which disturbs the electronic structure of the pristine CPPs and consequently leads to a single redshifted emission from the charge transfer (CT) state (Fig. 1a). Therefore, our objective is to obtain a D-A CPP that demonstrates two distinct, tunable emissions from two emissive states: a locally excited (LE) state for blue emission and a CT state for a significantly redshifted emission (as illustrated in Fig. 1). Achieving such a feat faces a significant challenge yet holds great appeal for the development of new applications, for instance, in the fields such as multicolor luminescent materials, particularly in the realm of single-molecule white-light emission.

Multicolor luminescence materials hold significant potential in white light-emitting diodes, flexible displays, information storage and bio-imaging[64–70]. The single-molecule organic white-light emission materials, featuring dual-emission peaks spanning 400-700 nm visible light region, exhibit a variety of advantages over multicomponent emitters. These advantages include good light reproducibility, no phase separation and reduced color degradation[71–73]. In principle, dual emission commonly originates from two emissive states: the lowest singlet excited state and one of the excited CT state[74,75], the lowest triplet excited state[76–78], or excimer state[79,80], which exhibits a largely redshifted emission. We proposed that by integrating acceptors with adjustable electron-withdrawing capacity into CPP, a single-molecular emitter could be created with inherent and adjustable dual-emission capabilities from LE and CT states when excited at single-wavelength, thus enabling the realization of multicolor including white-light emission (Fig. 1b). We expected that adjusting the LUMO levels of the D-A CPP nanohoop through acceptor engineering would enable us to manipulate the CT state and thus to control the optical properties,

which is crucial for creating D-A CPP nanohoops with enhanced optical and electrochemical characteristics.

To realize the aforementioned expectation, 1,4-benzoquinone, 1,4-naphthoquinone and 1,4-anthraquinone have been deliberately chosen as electron acceptors and annulated laterally onto one of benzenes in [10]CPP, rather than spanning across the CPP nanohoop (Fig. 1). This rational design not only retains the structural feature of CPP, but also endows quinone-based [10]CPPs with a CT state, thus leading to the formation of a built-in dual emission from LE and CT states at the single molecular level after single-wavelength excitation. Since quinone acceptors are not compatible with the reductive aromatization that is crucial for the synthesis of CPPs[1], a post-modification strategy was adopted to prepare these quinone-based [10]CPP nanohoops. To achieve this goal, thiophene-1,1-dioxide was selected as it is recognized for its versatility and effectiveness as a Diels−Alder diene, capable of engaging in a variety of reactions[81,82]. Herein, we present the quinone-based acceptor engineering of various D-A CPPs (**Nq[10]CPP, Aq[10]CPP** and **Tq[10]CPP**) through post-synthetic strategy based on Diels-Alder reaction of **oxTh[10]CPP** incorporating thiophene-1,1-dioxide (Figs. 1 and 2). Interestingly, these quinone-based D-A CPP nanohoops demonstrate a distinctive acceptor-dependent dual fluorescence emission in organic solvents when excited at single-wavelength, thus leading to multicolor emission. It is noteworthy that **Aq[10]CPP** exhibits single-molecular white-light emission in pure CHCl₃. Importantly, the ratio of dual-emission intensity in these D-A CPPs can be effectively regulated by multiple factors such as solvent polarity, aggregation states, and redox reaction, thus resulting in a diverse range of fluorescence emissions including white-light emission in single-molecule after single-wavelength excitation. Time-dependent density functional theory (TD-DFT) calculations reveal a significant lowering of the LUMO levels through the precise modifications of acceptors in these D-A nanohoops.
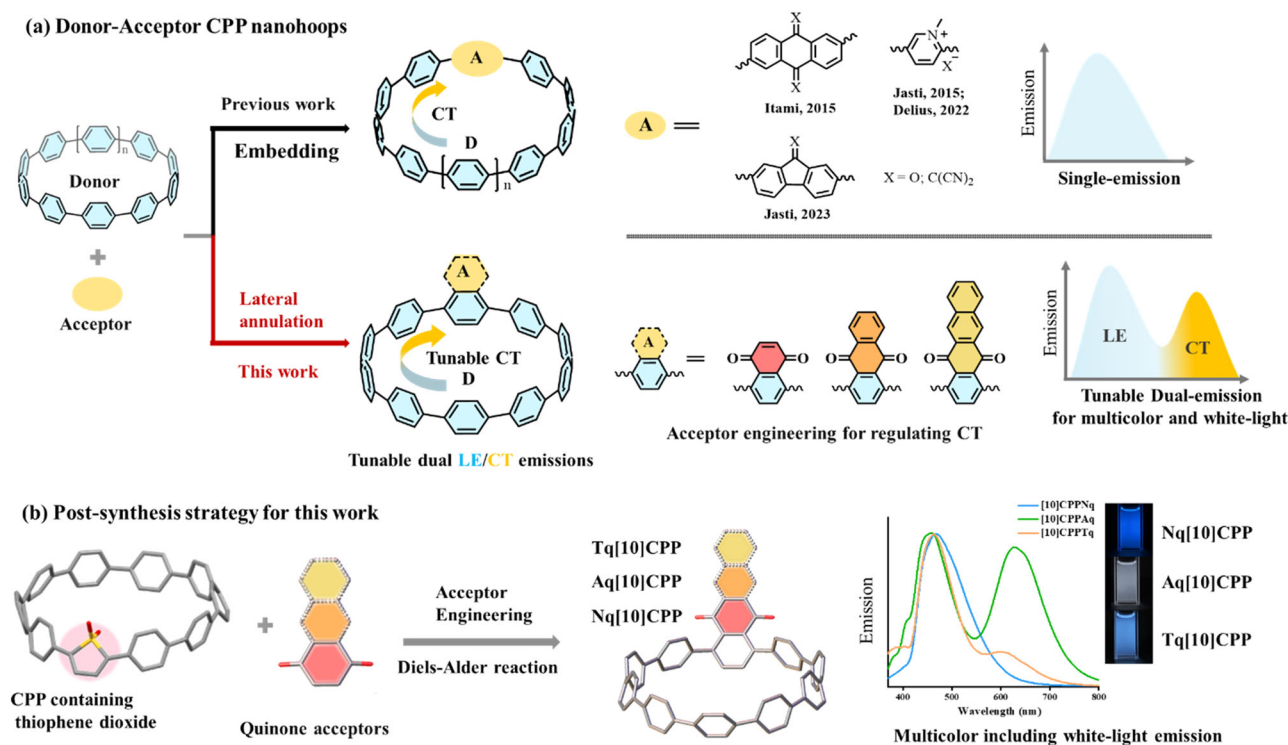

Fig. 1 | **Conceptional strategy for designing and constructing D-A CPP nanohoops with dual-emission states. a** The D-A CPP nanohoops exhibiting a single-emission in previous work (up) and a tunable dual-emission from the locally excited (LE) and charge transfer (CT) states in this work (bottom). **b** An effective post-synthesis strategy based on Diels-Alder reaction to synthesize quinone-based D-A [n]CPPs (Nq[10]CPP, Aq[10]CPP and Tq[10]CPP) and the fluorescence emission spectra in CHCl₃ in this work. Nq Naphthoquinone, Aq Anthraquinone, Tq Tetracenequinone.
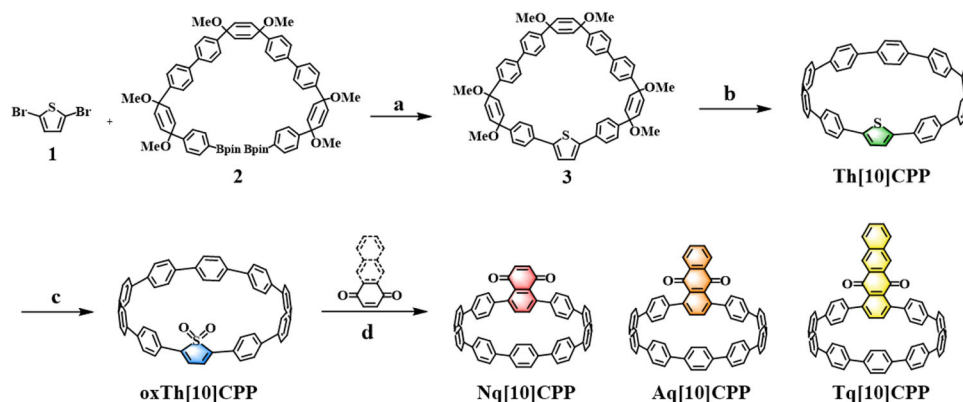
Fig. 2 | Synthetic route. Reaction conditions: **a** Pd(PPh₃)₄, K₂CO₃, THF/H₂O, 110 °C, overnight; **b** SnCl₂, HCl, THF, r.t., 16 h, 12 % in two steps; **c** (CH₃)₂CO, NaHCO₃, Oxone, dichloromethane, H₂O, -5 °C, 24 h, 33%; **d** phenyl ether, 200 °C, 2 days, 37%-51%. **Th** Thiophene. **oxTh** thiophene-1,1-dioxide.
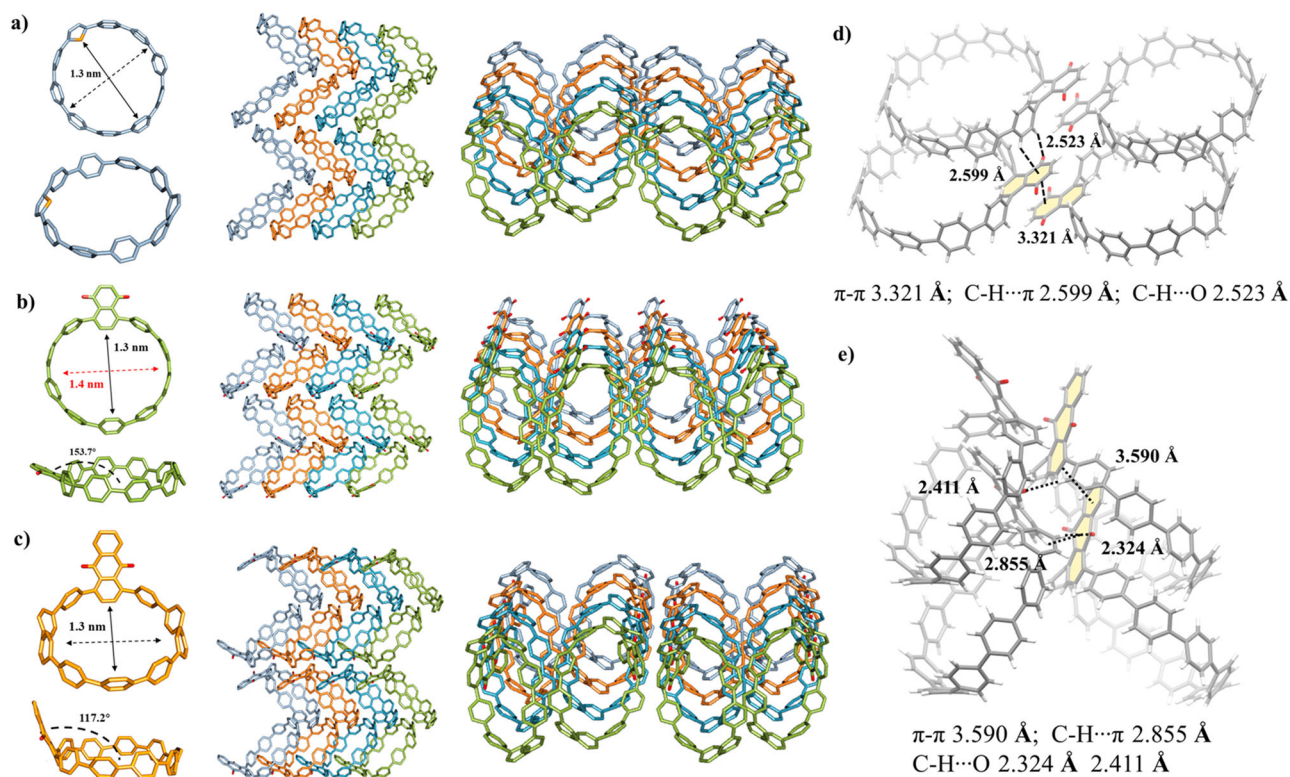

Fig. 3 | X-ray crystal structures. X-ray crystal structures (left), Herringbone packing model (middle), Long range channel alignment (right) of **a** Th[10]CPP, **b** Nq[10]CPP and **c** Aq[10]CPP; intermolecular noncovalent interactions of **d** Nq[10]CPP and e) **Aq[10]CPP**.

Results

Synthesis

Our synthetic strategy involves the synthesis of CPP nanohoop with a thiophene moiety (**Th[10]CPP**), which can be readily oxidized to yield **oxTh[10]CPP**. The post-synthesis of **oxTh[10]CPP** through Diels-Alder reaction with various quinones results in the formation of D-A CPPs (**Nq[10]CPP, Aq[10]CPP** and **Tq[10]CPP**). The synthetic procedures for five nanohoops are shown in Fig. 2. Initially, 2,5-dibromothiophene was coupled with C-shaped borate esters **2** by Suzuki-Miyaura cross-coupling in a diluted solution to obtain the macrocyclic precursor **3**, which was subsequently treated with the freshly prepared H₂SnCl₄ in anhydrous tetrahydrofuran at room temperature to afford the macrocycle **Th[10]CPP** with a yield of 12% over two steps. **oxTh[10]CPP** was then prepared by oxidizing **Th[10]CPP** in the presence of prepared dimethyldioxirane, with its structure unequivocally characterized by single crystal X-ray diffraction (Fig. 3a and S1). Finally, **Nq[10]**

CPP, Aq[10]CPP and **Tq[10]CPP** were synthesized via post-functionalization using Diels-Alder reactions of **oxTh[10]CPP** with 1,4-benzoquinone, 1,4-naphthoquinone and 1,4-anthraquinone, respectively, in phenyl ether at 200 °C with 37-51% yields for each nanohoop. The structures of these quinone-based [10]CPPs were characterized by ¹H NMR, ¹³C NMR and MALDI-TOF MS (Fig. S47-S66).

X-ray crystallographic analysis

The structures of **Th[10]CPP, Nq[10]CPP** and **Aq[10]CPP** were further confirmed by single-crystal X-ray analysis (Fig. 3, S1–S3 and Table S1-S3). Suitable crystals were obtained by slow diffusion of n-Hexane into dichloromethane solution at room temperature. Crystallographic studies indicate that **Th[10]CPP, Nq[10]CPP** and **Aq[10]CPP** feature nearly circular cavities with diameters of about 1.3 nm. All nanohoops adopt a herringbone packing mode, resulting the formation of tubular channels in the solid phase. However, **Nq[10]CPP** and **Aq[10]CPP**
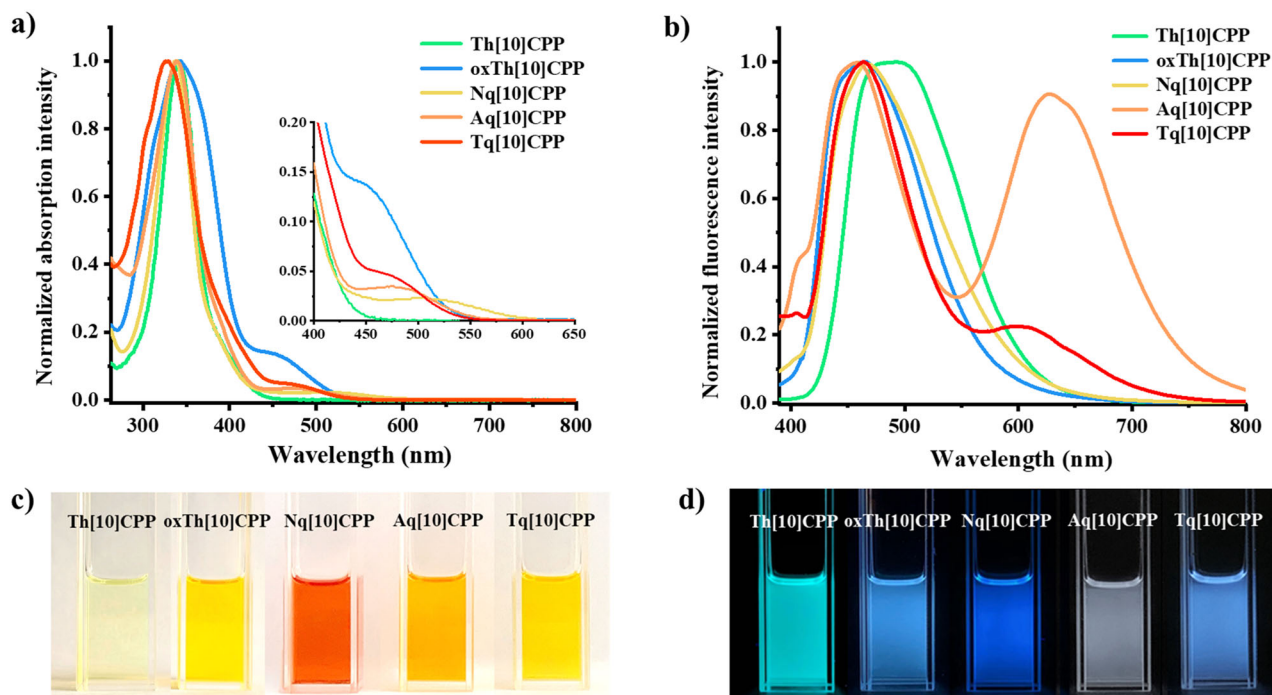
Fig. 4 | Photophysical Properties. The **a** UV-Vis spectra, **b** Fluorescence spectra of **Th[10]CPP, oxTh[10]CPP, Nq[10]CPP, Aq[10]CPP** and **Tq[10]CPP** (1.0 × 10⁻⁵ M) in CHCl₃, Pictures of **Th[10]CPP, oxTh[10]CPP, Nq[10]CPP, Aq[10]CPP** and **Tq[10]CPP** in CHCl₃ **c** at ambient light and **d** at λ = 365 nm.

exhibit distinct packing characteristics as shown in Figs. 3b and 2c. In particular, the quinone units display varying degrees of outward tilt relative to the cavity plane of CPP. For **Nq[10]CPP**, naphthoquinone moiety is positioned at a dihedral angle of 154° with respect to the cavity plane (Fig. 3b). This configuration promotes π − π stacking interaction between adjacent naphthoquinone moieties, with a contact distance of 3.3 Å. The overlapped area of two neighboring naphthoquinone moieties is estimated to be approximately 61%, indicating a strong π⋯π interaction (Fig. 3d). In the case of **Aq[10]CPP**, the anthraquinone unit is tilted at a smaller dihedral angle of 117° relative to the cavity plane, which differs notably from **Nq[10]CPP** (Fig. 3c). This reduced tilt angle results in the intercalation of anthraquinone moieties within adjacent CPP cavities in the solid phase (Fig. 3e). This arrangement contrasts sharply with **Nq[10]CPP**, where the π − π stacking between two adjacent naphthoquinone moieties occurs at the outer cavity. Additionally, both **Nq[10]CPP** and **Aq[10]CPP** single crystals feature numerous intermolecular hydrogen bonds (C-H⋯O at distances of 2.523 Å, 2.324 Å and 2.411 Å; C- H⋯π at distances of 2.599 Å and 2.855 Å) between the quinone and phenylene segments. Furthermore, the unit cells of **Th[10]CPP, Nq[10]CPP** and **Aq[10]CPP** belong to the monoclinic P2₁/c, C2/c and P2₁ space groups, respectively (Table S1-S3).

Photophysical Properties

The optical properties of five [10]CPP derivatives in this work were examined by UV-Vis absorption spectroscopy, fluorescence emission spectroscopy and time-resolved fluorescence decay (Fig. 4, S5 and S8). The key data were compiled in Table 1. To establish a connection between the electronic structure and photophysical properties, TD-DFT calculations were performed at the MN15/6-31 G*/SMD level. The UV-Vis absorption spectra of the acceptor-based CPPs **oxTh[10]CPP, Nq[10]CPP, Aq[10]CPP** and **Tq[10]CPP** in chloroform displayed comparable absorption maxima (λ_{max}) around 329-343 nm, accompanying by a red-shifted broad band ranging from 430 nm to 620 nm (Fig. 4a). These absorption maxima were very close to that of **[10]CPP** (338 nm)[3]. According to the DFT calculations, the main absorption

peak can be attributed to the HOMO-1 → LUMO transition for **oxTh[10] CPP** at 343 nm, HOMO-1 → LUMO + 1 and HOMO → LUMO + 2 transitions for **Nq[10]CPP** at 338 nm, HOMO-1 → LUMO + 1 and HOMO → LUMO + 3 transitions for **Aq[10]CPP** at 339 nm, and HOMO → LUMO + 3 and HOMO-1 → LUMO + 2 transitions for **Tq[10]CPP** at 329 nm (Fig. 5). The red-shifted broad bands in these spectra can be ascribed to the characteristic absorption peaks of the ICT states mainly associated with the transitions of HOMO-2 → LUMO and HOMO → LUMO, indicating the formation of D-A CPPs (Table S11 and S15). Additionally, as shown in Fig. 5, the HOMOs of **oxTh[10]CPP, Nq[10] CPP, Aq[10]CPP** and **Tq[10]CPP** were predominantly located on the donor phenylene backbone, while the LUMOs were mainly situated on thiophene-1,1-dioxide and quinone acceptors, respectively. Notably, despite the HOMO energies of these D-A CPPs being around 5.830 eV, close to that of **[10]CPP**, the LUMO energies of these D-A CPPs are obviously lower: -1.880 eV for **oxTh[10]CPP**, -1.967 eV for **Tq[10]CPP**, -2.074 eV for **Aq[10]CPP**, and -2.310 eV for **Nq[10]CPP**. These values are significantly lower than that of **[10]CPP** (-1.072 eV), leading to a narrower HOMO-LUMO band gap in these D-A nanohoops (Table S18). However, the UV-Vis absorption spectrum of **Th[10]CPP** only showed a main absorption peak at 341 nm, attributed to the transitions of HOMO-2 → LUMO and HOMO → LUMO + 2 (Table S11). Furthermore, based on the onset of the longest wavelength absorption (λ_{onset}), the optical gaps of **Th[10]CPP, oxTh[10]CPP, Nq[10]CPP, Aq[10]CPP** and **Tq[10]CPP** were estimated to be 2.87, 2.34, 2.02, 2.24 and 2.31 eV, respectively (Table 1). This trend of the optical gap variation aligned with the theoretical calculations (Table S18).

Subsequently, the fluorescence emission spectroscopies in solution were also conducted (Figs. 4b and 4d). Interestingly, in chloroform, the emission spectrum of **Aq[10]CPP** exhibits two obvious peaks with comparable intensities at 460 and 628 nm, resulting in the emission of a near white light with a CIE coordinate (0.33, 0.25). Similarly, **Tq[10]CPP** displayed a strong emission peak at 465 nm, along with a redshifted peak at 598 nm with lower intensity, leading to sky blue emission. Unexpectedly, **Nq[10]CPP** exhibited a main emission peak at 465 nm, no obvious redshifted emission was detected.

Table 1 | The photophysical and electrochemical data of Th[10]CPP, oxTh[10]CPP, Nq[10]CPP, Aq[10]CPP and Tq[10]CPP

	$\lambda_{abs}^{a, b}$ (nm)	$\lambda_{em}^{a, c}$ (nm)		Φ_F^{d} (%)	τ^{e} (ns)	$E_{g(opt)}^{f}$ (eV)	$E_{1/2}^{ox}$ (eV)	$E_{1/2}^{red}$ (eV)	E_{HOMO}^{g}(eV)	E_{LUMO}^{h}(eV)
		Solution	Film							
Th[10]CPP	341	493	487	17.4	$\tau = 1.3$	2.87	0.77	-1.65, -2.41	-5.53	-3.42
oxTh[10]CPP	343, 430-560	464	570	4.0	$\tau = 2.6$	2.34	1.05	-1.55, -2.43	-5.58	-3.49
Nq[10]CPP	338, 450-620	465	440, 662	0.7	$\tau_1 = 0.5$ (78.8 %) $\tau_2 = 3.4$ (21.2 %)	2.02	0.99	-1.51, -2.00	-5.57	-3.57
Aq[10]CPP	339, 440-550	460, 628	446, 600	1.3	$\tau_1 = 0.4$ (85.6 %) $\tau_2 = 4.0$ (14.4 %)	2.24	0.78	-1.58, -2.18	-5.59	-3.53
Tq[10]CPP	329, 450-550	465, 598	462, 568	1.2	$\tau_1 = 0.5$ (91.1 %) $\tau_2 = 4.7$ (8.9 %)	2.31	0.64	-1.56, -2.04	-5.52	-3.63

[a]UV-Vis absorption and fluorescence spectra were measured in $CHCl_3$ (1×10^{-5} M) at room temperature.
[b]Wavelength of the maximum absorption.
[c]Emission maximum (λ_{ex}=highest intensity of absorption).
[d]Absolute fluorescence quantum yield.
[e]Lifetime in $CHCl_3$ solution (X^2 = 1.128, 1.002 and 1.117 for Nq[10]CPP, Aq[10]CPP and Tq[10]CPP, respectively,).
[f]Estimated from absorption onset, $E_{g(opt)} = 1240/\lambda_{onset}$.
[g]E_{HOMO} = -(4.8+E_{onset}^{ox}) eV (calibration by ferrocene).
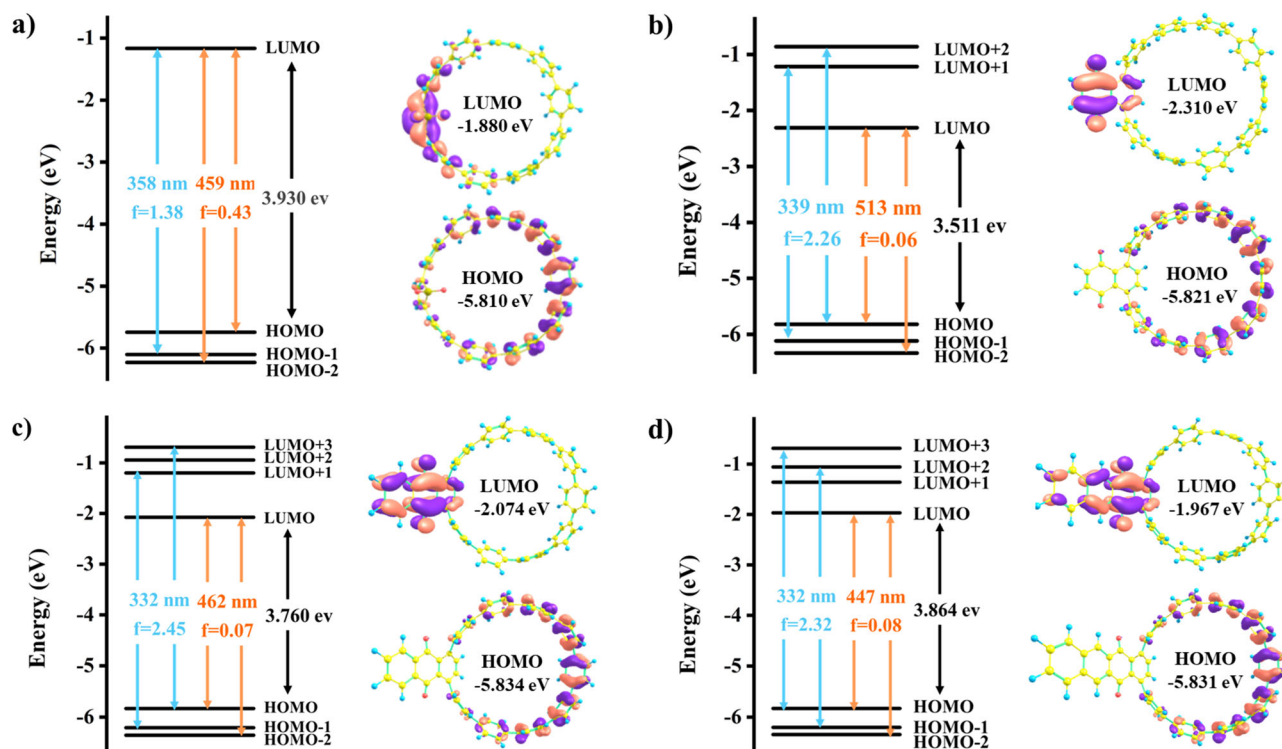[h]E_{LUMO} = -(4.8+E_{onset}^{red}) eV (calibrated by ferrocene).

Fig. 5 | Theoretical calculations. Energy diagrams and pictorial representations of the frontier molecular orbitals for **a** oxTh[10]CPP, **b** Nq[10]CPP, **c** Aq[10]CPP and **d** Tq[10]CPP calculated by TD MN15/6-31 G*/SMD. The values of *f* represent the oscillator strengths.

This phenomenon can be attributed to the fact that 1,4-naphthoqui-none moiety in **Nq[10]CPP** is more exposed to solvent than other quinone units in **Aq[10]CPP** and **Tq[10]CPP**, which renders the red-shifted emission of **Nq[10]CPP** more sensitive to the polarity of solvents. Pleasingly, the redshifted emission of **Nq[10]CPP** was observed in a nonpolar solvent (vide infra). It is noteworthy that the quinone-based [10]CPPs exhibit distinct characteristics of a built-in dual emis-sion at the single molecular level after single wavelength excitation, which is sharply different from the other reported D-A [n]CPPs[57–63]. It is worth noting that the emission wavelengths of Nq[10]CPP (465 nm), Aq[10]CPP (460 nm) and Tq[10]CPP (465 nm) at blue wavelength are all close to that of [10]CPP (466 nm)[3]. Accordingly, the emission at blue wavelength can be attributed to the LE state, similar to [10]CPP.

Furthermore, theoretic calculations of excited-states revealed that the quinone-based [10]CPPs possess dual emission from LE and CT states. For instance, the blue emission peak of **Aq[10]CPP** at 460 nm is attributed to transitions from LUMO + 2 → HOMO and LUMO + 1 → HOMO-1, corresponding to the LE state of oligophenylene backbone, while the redshifted emission peak at 628 nm is assigned to the tran-sition of LUMO → HOMO, which is attributed to the CT state between oligophenylene backbone and anthraquinone (Table S17). The same argument holds for **Tq[10]CPP** and **Nq[10]CPP**. In contrast, **oxTh[10] CPP** exhibits a single emission peak at 464 nm in chloroform without a redshifted emission peak even in nonpolar solvents, indicating the absence of CT state (Figure S6). Additionally, **Th[10]CPP** also displays one peak at 493 nm. Theoretic calculations revealed that the emission

at 464 nm of **oxTh[10]CPP** primarily arises from the LUMO + 1 → HOMO transition, while the emission at 493 nm of **Th[10]CPP** is mainly due to the LUMO → HOMO-1 transition. These transitions are attributed to the LE state but no transition for CT states was revealed for **Th[10]CPP** and **oxTh[10]CPP** (Table S13). In addition, the fluorescence transient decay spectra of **Th[10]CPP** and **oxTh[10]CPP** only showed a prompt decay with a lifetime of 1.3 ns and 2.6 ns, respectively (Table 1 and Figure S5). While the quinone-based [10]CPPs exhibited a double-exponential decay feature, composing of a short-lived species with a lifetime of about 0.5 ns and a long-lived species with a lifetime of about 4.0 ns (Table 1 and Figure S8). The fluorescence quantum yields of **Th[10]CPP**, **oxTh[10]CPP**, **Nq[10]CPP**, **Aq[10]CPP** and **Tq[10]CPP** were measured and listed in Table 1. Furthermore, phosphorescence emissions of **Nq[10]CPP**, **Aq[10]CPP** and **Tq[10]CPP** were observed at about 650 nm for **Aq[10]CPP** and **Tq[10]CPP** at 77 K in 2- methyltetrahydrofuran (Figure S10-S12), with lifetimes of 15.8 and 30.5 ms, respectively. In contrast, no phosphorescence was detected for **Nq[10]CPP** under the same conditions.

Given **Nq[10]CPP**, **Aq[10]CPP** and **Tq[10]CPP** exhibit the D-A characteristics of CT state, solvatofluorochromic behavior were expected. Subsequently, fluorescence spectra of **Nq[10]CPP**, **Aq[10]CPP** and **Tq[10]CPP** were further measured in various solvents including tetrachloromethane (CCl_4), tetrahydrofuran (THF) and dimethyl sulfoxide (DMSO) (Figure S9 and Table S6). **Aq[10]CPP** shows obvious dual-emissions at 453 nm and 580 nm in nonpolar solvent CCl_4 with an intensity ratio of the redshift emission to the blue one to be 1.6 (Table S8). In THF, the blue emission wavelength of **Aq[10]CPP** did not exhibit obvious changes, while the emission peak at longer wavelength displays a redshift to 600 nm, and the intensity ratio of the dual-emission decreases to 0.4 (Table S8). Variations in the dual-emission intensities caused by the polarity of solvents eventually led to the multicolor emissions, including pale purplish-pink, white and blue (Figure S9e and S9f). Similarly, **Nq[10]CPP** and **Tq[10]CPP** also display two emission peaks in CCl_4 (Figure S9b and S9h). In THF, **Tq[10]CPP** show a main peak at 465 nm accompanying with a shoulder peak at 600 nm. However, the emission peak of **Nq[10]CPP** at longer wavelength is quenched. Additionally, the emissions of these CPPs at longer wavelengths were all markedly quenched in DMSO. These observations further support the fact that the emission peaks at blue wavelength are attributed to the LE state, whereas the peaks at red-shifted wavelength are associated with the CT state, which is notably influenced by the solvent polarity. Furthermore, we also calculated the dipole moments of excited states using the Lippert Mataga formalism, thereby verifying the presence of the LE and CT states (Table S19-S24 and Figure S42-S46).

Aggregations in THF/H$_2$O and the Film of PMMA

Encouraged by the aforementioned results, we were motivated to explore the potential of D-A nanohoops as a single-molecular emitter for full-color emission, including white-light emission upon aggregation. The luminescence properties were further investigated in THF with different water fractions (f_w) (Fig. 6). As shown in Fig. 6b, **Aq[10]CPP** exhibits emission peaks at 457 nm and 600 nm in pure THF. As the water content increased from 0% to 50%, the fluorescence intensity at 457 nm gradually decreased, while that at 600 nm remained relatively constant. When the water content exceeds 53%, the intensity of emission peak at 600 nm steadily increases as the water fraction rises. The maximum emission was observed at f_w = 80 %, eventually accompanying with disappearance of the emission peak at 464 nm. Moreover, the fluorescent color of solution transitions from blue to orange, covering a region near white light with a CIE coordinate of (0.33, 0.26) at f_w = 55%. Furthermore, the Tyndall effect, which refers to the scattering of light by particles suspended in a colloid or fine suspension[83], was observed in our experiments. Specifically, the Tyndall phenomena were detected as the water fraction increases from 50% to 90%,

indicating that aggregation occurred in the mixed solvents (Figure S17). Moreover, the dynamic light scattering (DLS) investigations suggested that nanoparticles were formed with sizes ranging approximately from 111 nm to 1793 nm, dependent on the water fractions (Figure S18). As shown in Figs. 6a and 6c, the fluorescence spectra of **Nq[10]CPP** and **Tq[10]CPP** follow a similar trend. As the water content increased, the fluorescence intensity of **Nq[10]CPP** decreased at 465 nm, while a new emission peak appeared at 667 nm with enhanced fluorescence intensity. For **Tq[10]CPP**, it shows a major emission peak at 465 nm accompanying with a shoulder peak at 600 nm in pure THF. At f_w = 0%-70%, the fluorescence intensity at 465 nm decreased markedly, whereas the intensity at 600 nm showed little variation. When the water fraction is over 70%, the emission intensity at 600 nm is obviously enhanced. These spectral changes in the mixture of THF/H$_2$O lead to the significant changes in the emission color from blue to red for **Nq[10]CPP** and from blue to orange for **Tq[10]CPP**, respectively. The Tyndall phenomena were also observed when the water fractions were beyond 70% and 60% for **Nq[10]CPP** and **Tq[10]CPP**, respectively. The formations of nanoparticles were further demonstrated by DLS experiments (Figure S15-S16 and S19-S20). More importantly, **Tq[10]CPP** show the dual-emissive feature and emit white light with the CIE coordinates of (0.33, 0.28) at f_w = 72 %. As for **oxTh[10]CPP**, it exhibits blue emission at 464 nm in pure THF (Fig. 6d). When the water fraction exceeds 55 %, a new emission peak emerges at 575 nm, with its intensity steadily increasing while the emission intensity at 464 nm decreases. The appearance of a new peak at 575 nm is also associated with the Tyndall phenomenon and the formation of nanoparticles as indicated by DLS (Figure S13-S14). Simultaneously, the fluorescent color of solution changes significantly from blue to yellow, covering a region near white light with a CIE coordinate of (0.32, 0.30) at f_w = 60%. The intensity ratios of the red-shift emission to the blue one in all these CPPs can be precisely adjusted through aggregation, ranging from 0 (f_w = 0 %) to a maximum of 70 (f_w = 90 %) (Fig. 6, middle). For quinone-based CPPs, the spectral changes observed in THF/H$_2$O indicate that aggregation substantially facilitates the emission of CT states. As for **oxTh[10]CPP**, the emission at red-shifted wavelength after aggregation is speculated to the formation of the intermolecular charge transfer.

In order to study the morphology of aggregated [10]CPPs, scanning electron microscopy (SEM) was employed (Fig. 7 and S21-S24). SEM images demonstrated that the morphologies of the nanoparticles varied as the water fraction was adjusted. For **Aq[10]CPP**, fibrous aggregates initially form at 50% water fraction (Figure S19a). At 90% water fraction, the morphology is characterized by smooth, angular regular polyhedra (Fig. 7d). As the water fraction increases, the morphologies of **Nq[10]CPP**, **Tq[10]CPP** and **oxTh[10]CPP** transition from sphere to square and finally to polyhedron. (Figure S21, S22 and S24).

Next, we explored solid-state emission through film fabrication (Fig. 8 and Table 1). We prepared the films by dispersing 5.0 wt.% weight fractions of each nanohoop into the poly(methylmethacrylate) (PMMA) matrix. The emission spectra of the acceptor-based [10]CPPs in films exhibited significant differences compared to those observed in solution. Particularly, the quinone-based [10]CPP display dual-emission peaks at 440 and 662 nm for **Nq[10]CPP**, 446 and 600 nm for **Aq[10]CPP** and 462 and 568 nm for **Tq[10]CPP**. Moreover, compared to those in solution, the emissions at the longer wavelength were notably enhanced in the PMMA films, with an intensity ratio of the redshift emission to the blue one to be 0.8, 8.2 and 2.1 for **Nq[10]CPP**, **Aq[10]CPP** and **Tq[10]CPP**, respectively (Table S8). Upon excitation at 365 nm, the films of **Nq[10]CPP**, **Aq[10]CPP** and **Tq[10]CPP** emit red, orange and yellow emission, respectively. On the other hand, **oxTh[10]CPP** exhibits a red-shifted emission at 570 nm, producing a yellow color. In contrast, **Th[10]CPP** demonstrates a green emission at 487 nm, similar to its behavior in solution. These findings clearly
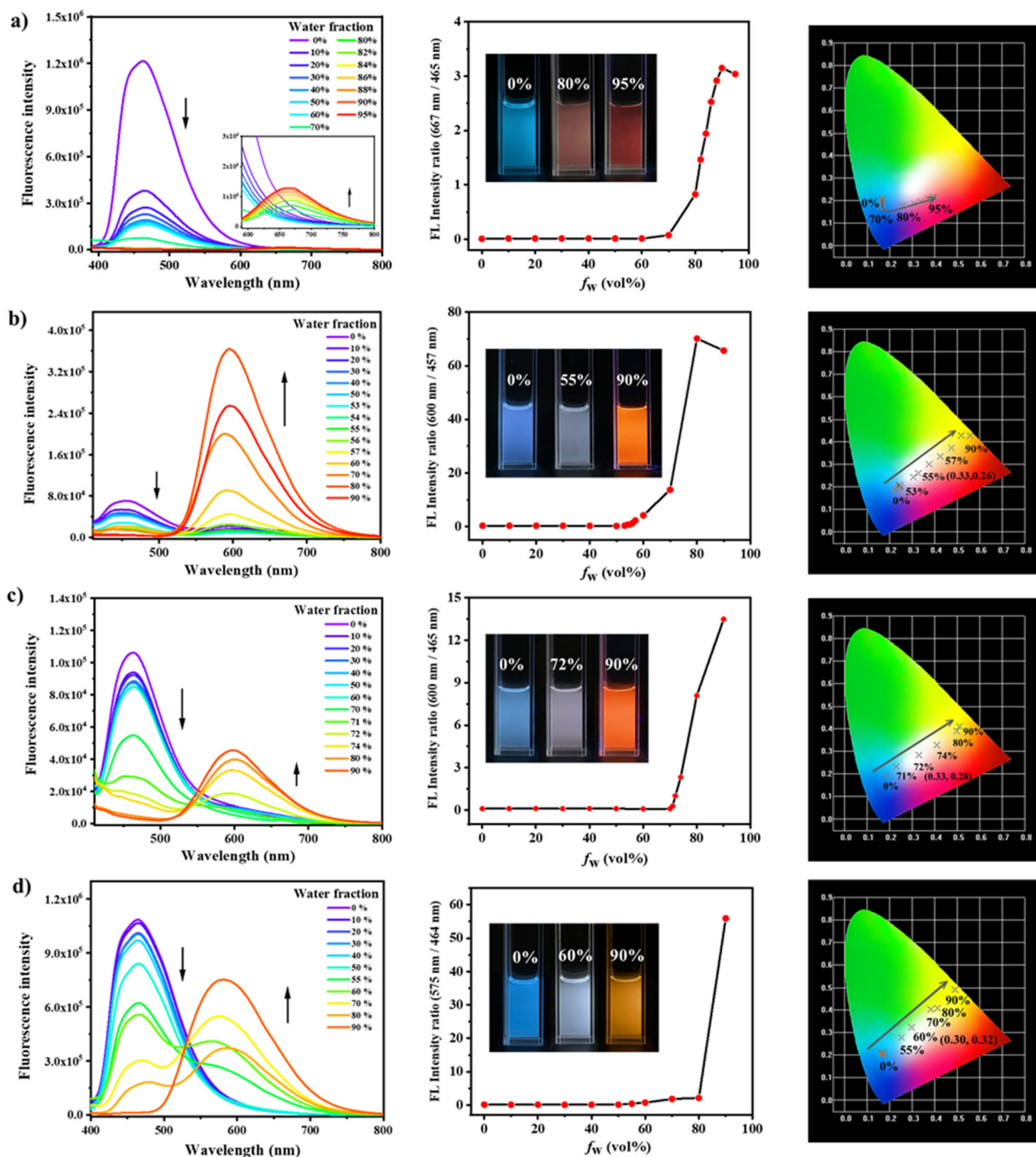
Fig. 6 | Aggregations in THF/H2O. Fluorescence emission spectra with different water fraction in THF solvent (left), Curve of fluorescent intensity ratio of the redshifted emission to the blue one vs. water fraction. Insert: photos of changes in fluorescence color at λ = 365 nm (middle), and CIE 1931 chromaticity diagram in THF/H$_2$O mixtures (right) of (**a**) **Nq[10]CPP** (1.0 × 10^{-5} M, λ$_{ex}$ = 338 nm), **b Aq[10] CPP** (5.0 × 10^{-6} M, λ$_{ex}$ = 331 nm), **c Tq[10]CPP** (5.0 × 10^{-6} M, λ$_{ex}$ = 332 nm), **d oxTh[10]CPP** (1.0 × 10^{-5} M, λ$_{ex}$ = 343 nm).

indicate that manipulating acceptors in these D-A [10]CPPs readily enables the achievement of multicolor, including white-light emission both in isolated and aggregated states.

Electrochemical Properties and Redox
The electrochemical properties were investigated by cyclic voltammetry (CV) and differential pulse voltammetry (DPV) (Figure S25 and Table S9). **Th[10]CPP** exhibits irreversible oxidation processes at 0.77 V and two reduction processes with quasi-reversible peaks at -1.65

and -2.41 V. **oxTh[10]CPP** exhibits an oxidation peak at 1.05 V and two irreversible reduction processes at -1.55 and -2.43 V. As for quinone-based [10]CPPs, irreversible oxidation peaks were observed for **Nq[10] CPP** at 0.99 V, **Aq[10]CPP** at 0.78 V and **Tq[10]CPP** at 0.64 V (Figure S25), indicating an obvious acceptor-dependent oxidation potentials. On the other hand, two reduction peaks were detected at about -1.50 V and -2.00 V, attributable to the introduction of quinone. Given the facile reducibility of quinone, its reduction can serve as a stimulus for effectively modulating the properties of the quinone-based [10]
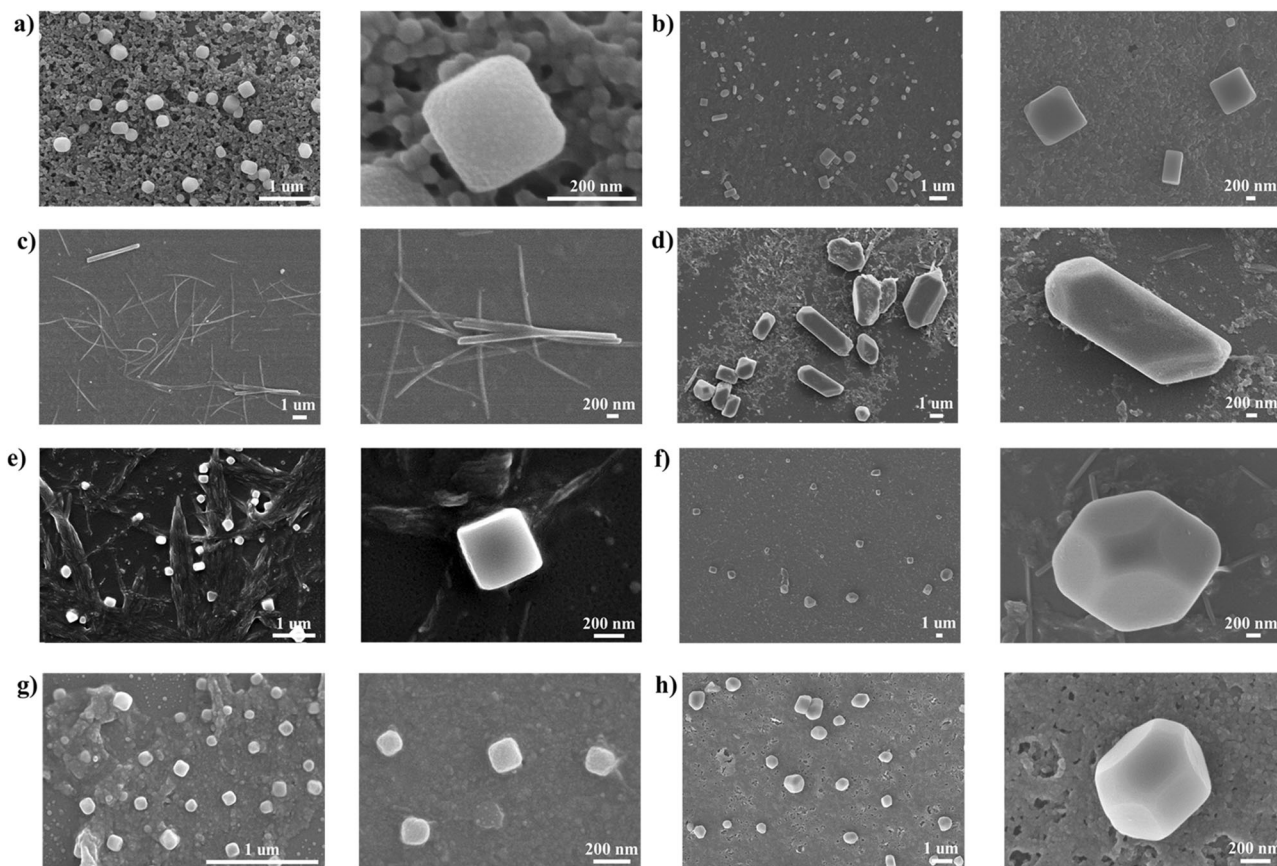
Fig. 7 | Scanning electron microscopy. The SEM images of **a** Nq[10]CPP in THF/water (20:80, v/v, f_w = 80 %); **b** Nq[10]CPP in THF/water (5:95, v/v, f_w = 95 %); **c** Aq[10]CPP in THF/water (45:55, v/v, f_w = 55 %); **d** Aq[10]CPP in THF/water (5:95, v/ v, f_w = 90 %); **e** Tq[10]CPP in THF/water (28:72, v/v, f_w = 72 %); f) Tq[10]CPP in THF/ water (10:90, v/v, f_w = 90 %). **g** oxTh[10]CPP in THF/water (40:60, v/v, f_w = 60 %); h) oxTh[10]CPP in THF/water (10:90, v/v, f_w = 90 %).
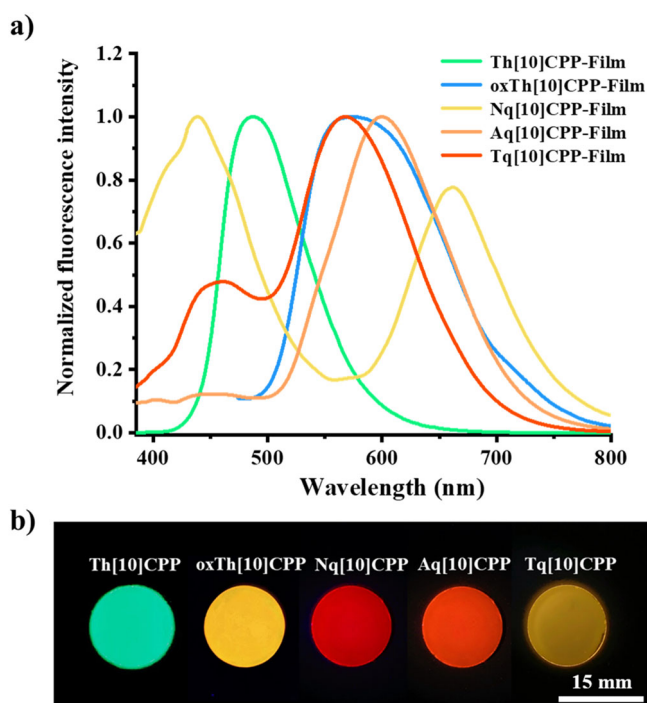

Fig. 8 | Emission spectra and colors in PMMA films. a The Fluorescence spectra of 5.0 wt.% **Th[10]CPP, oxTh[10]CPP, Nq[10]CPP, Aq[10]CPP** and **Tq[10]CPP** / PMMA films, **b** Pictures of **Th[10]CPP, oxTh[10]CPP, Nq[10]CPP, Aq[10]CPP** and **Tq[10]CPP** in PMMA films at λ = 365 nm.

CPPs. Subsequently, **Aq[10]CPP** was selected and chemically reduced using NaBH$_4$ in a mixed solution of THF and MeOH to produce **red-Aq[10]CPP** containing anthracenediol (characterized by ^{1}H NMR, Figure S57). The modulation of optical properties through chemical reduction was carried out by the UV-Vis absorption spectroscopy and fluorescence emission spectroscopy in CHCl$_3$ (Fig. 9). The absorption spectrum of **red-Aq[10]CPP** exhibits a prominent peak at 334 nm, while the absorption band at the range from 440 to 620 nm corresponding to the ICT state is absent compared to **Aq[10]CPP**. Simultaneously, the solution undergoes a color transition from orange to light yellow. Meanwhile, the **red-Aq[10]CPP** exhibits a maximum emission peak at 460 nm, very close to the LE emission in **Aq[10]CPP**, while the emission of CT state at 629 nm becomes imperceptible, resulting in a significant change in fluorescence color from white to blue.

Discussion

In summary, a series of quinone-based [10]CPPs (**Nq[10]CPP, Aq[10] CPP** and **Tq[10]CPP**) have been successfully synthesized by an effective post-synthetic strategy using Diels-Alder reaction of **oxTh[10]CPP**. This versatile synthetic strategy, facilitated by the high reactivity of thiophene-1,1-dioxides, offers significant advantages in the efficient synthesis of various functionalized CPP nanohoops. Single-crystal analysis reveals that different acceptors allow for various intermolecular interactions between CPP nanohoops, leading to diverse stacking modes. Experimental results and theoretical calculations indicate that quinone-based [10]CPP nanohoops exhibit distinct D-A characteristics with a narrowed HOMO-LUMO band gap. Moreover, their photophysical properties can be regulated by the acceptor quinone. All quinone-based CPPs exhibit inherent dual-emission in purely organic solvents,
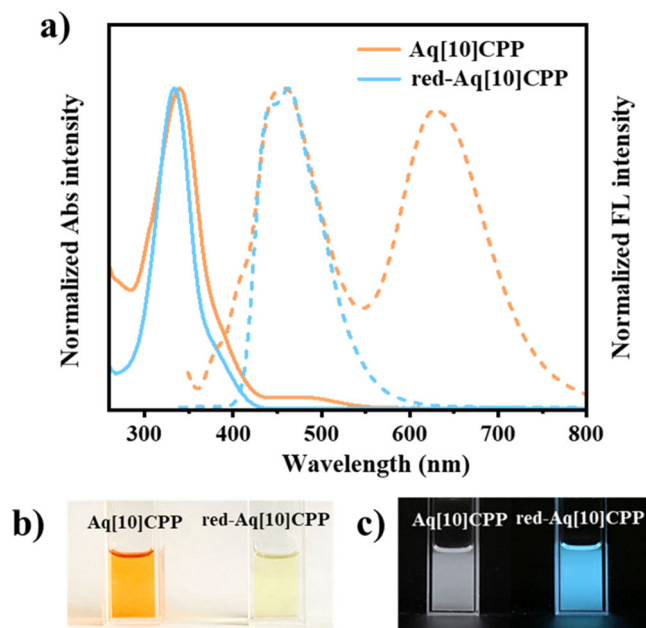
Fig. 9 | Photophysical properties of Aq[10]CPP upon reduction. a The UV-Vis spectra and Fluorescence emission spectra of **Aq[10]CPP** and **red-Aq[10]CPP** in CHCl₃. **b** Pictures of **Aq[10]CPP** and **red-Aq[10]CPP** in CHCl₃ under **b** ambient light and **c** UV light at λ = 365 nm. red: reduction.

attributed to the LE and CT states. It is noteworthy that **Aq[10]CPP** shows single-molecular white-light emission in CHCl₃. Furthermore, the intensity ratio of the dual-emission peaks can be adjusted by solvent polarity, aggregation and chemically reduction, emitting a wide range of fluorescent colors, including white light. We anticipate this study can provide valuable insights into the efficient synthesis of nanohoops with a broad range of properties and applications.

Methods

All starting chemicals were obtained from commercial sources and used without further purification, unless indicated otherwise. All reactions were performed with dry solvents under Argon in dried glassware with standard vacuum-line techniques. Anhydrous THF and 1,4-dioxane were obtained from the Solvent Purification System. NMR spectra were obtained with JEOL Delta (400 MHz and 600 MHz) spectrometer at 298 K, using dichloromethane-d (CD₂Cl₂) and chloroform-d (CDCl₃) as solvent. Mass spectra of MALDI-TOF were acquired on Bruker Daltonics Autoflex III. UV-Vis spectra were recorded on Shimadzu UV-2450. Fluorescence and phosphorescence spectra were measured on FS5 and Edinburg FLS-980 fluorescence spectrometer. The absolute fluorescence quantum yield was measured by using an absolute PL quantum yield spectrometer (Quantaurus-QY C11347-11). Scanning electron microscopy (SEM) was performed on a Hitachi SU-8000 with an accelerating voltage of 5 kV. Cyclic voltammetry (CV) and differential pulse voltammetry (DPV) experiments were carried out at room temperature with an electrochemical workstation from Chenhua Instruments Co. (Shanghai, China). Cyclic voltammetry (CV) and differential pulse voltammetry (DPV) were measured with a glass carbon electrode for THF solution of a sample (1 mM) in the presence of a supporting electrolyte (Bu₄NPF₆, 0.1 M) under nitrogen atmosphere and the scan rates at 100 mV/s. The potential was externally calibrated against the Fc/Fc⁺ couple versus a Ag electrode.

Synthesis of Th[10]CPP

To a dried 250 mL flask containing a magnetic stirring bar were added **1** (50 mg, 0.21 mmol, 1.0 eq), **2** (237 mg, 0.21 mmol, 1.0 eq), Pd(PPh₃)₄ (48 mg, 0.04 mmol, 0.2 eq) and K₂CO₃ (4.1 g, 30 mmol, 144.2 eq). The

flask was evacuated and filled with argon three times. Dry THF (45 mL) and the degassed distilled water (15 mL) was added via syringe. Then, the mixture was deoxygenated and freeze-pump-thawed (3×) and then was allowed to react at 110 °C overnight. After the reaction mixture was cooled, the mixture was extracted with ethyl acetate, washed with water and saturated brine. The combined organic phase was dried over sodium sulfate and consequently concentrated under reduced pressure. The crude product was initially purified by column chromatography on silica gel (petroleum ether/ethyl acetate = 4/1, v/v) to afford a yellow solid as the crude macrocyclic precursor that was used in the next step without further purification.

A H₂SnCl₄/THF solution was freshly prepared by dissolving anhydrous SnCl₂ (217 mg, 1.15 mmol) in 15 mL anhydrous THF under Ar atmosphere and then adding concentrated HCl (aq) (3 mL) to the solution. The resulting solution was deoxygenated and stirred for 30 min. Crude product (91 mg) was dissolved in anhydrous THF (38 mL) under the Ar atmosphere and the freshly prepared H₂SnCl₄/THF solution was added to this solution. The reaction mixture was stirred at room temperature for 24 h before being quenched with NaOH/H₂O solution. The aqueous layer was extracted with dichloromethane and the organic layers were combined and dried with anhydrous sodium sulfate. After purifying by column chromatography on silica gel (petroleum ether/CH₂Cl₂ = 2/1, v/v) to get **Th[10]CPP** as a yellow solid (Yield: 19 mg, 12 % in two steps). M.p. > 300 °C. ¹H NMR (600 MHz, CDCl₃, 298 K) δ: 7.59-7.55 (m, 28H), 7.53 (d, J = 8.6 Hz, 4H), 7.40 (d, J = 8.6 Hz, 4H), 7.17 (s, 2H). ¹³C NMR (150 MHz, CDCl₃, 298 K) δ: 148.0, 139.2, 138.6, 138.5, 138.3, 138.3, 133.7, 127.6, 127.6, 127.5, 127.4, 122.5. HR-MS (MALDI-TOF) calculated for C₅₈H₃₈S M: 767.2694, found 767.2773.

Synthesis of oxTh[10]CPP

(Method A) **Th[10]CPP** (50 mg, 0.064 mmol, 1.0 eq) was dissolved in acetone-H₂O-CH₂Cl₂ (1:1:1, 18 mL) in a two-necked 50 mL glass round bottom flask and added NaHCO₃ (862 mg, 10.26 mmol, 158.4 eq). The solution was stirred at -5 °C for 15 min. Then, the oxone (881.2 mg, 1.44 mmol, 22.1 eq) was added in 5 times and stirred at -5 °C for 14 h. The reaction was quenched with NaHSO₃, and extracted with dichloromethane. The organic layer was washed with brine and dried over anhydrous sodium sulfate. After purifying by column chromatography on silica gel (petroleum ether/CH₂Cl₂ = 1/2, v/v) to get **oxTh[10]CPP** as an orange solid (Yield: 16.9 mg, 33 %).

(Method B) To a dried 5 mL Schlenk containing a magnetic stirring bar was added **Th[10]CPP** (10 mg, 0.013 mmol, 1.0 eq) and the flask was evacuated and filled with argon three times. Subsequently, CH₂Cl₂ (0.5 mL), HCO₂H (50 μL) and H₂O₂ (100 μL, aq. 30%) were added via syringe at -5 °C and stirred for 1 h. Then, the mixture was allowed to react at 50 °C overnight. The reaction was extracted with dichloromethane. The organic layer was washed with brine and dried over anhydrous sodium sulfate. After purifying by column chromatography on silica gel (petroleum ether/CH₂Cl₂ = 1/2, v/v) to get **oxTh[10]CPP** as an orange solid (Yield: 2.5 mg, 24 %). M.p. > 300 °C. ¹H NMR (600 MHz, CDCl₃, 298 K) δ 7.63 (d, J = 8.8 Hz, 4H), 7.58 (d, J = 6.5 Hz, 28H), 7.53 (d, J = 8.8 Hz, 4H), 6.87 (s, 2H). ¹³C NMR (150 MHz, CDCl₃, 298 K) δ: 143.2, 141.4, 139.3, 138.7, 138.4, 138.3, 138.2, 138.1, 137.8, 128.9, 127.9, 127.7, 127.7, 127.6, 125.9, 119.6. HR-MS (MALDI-TOF) calculated for C₅₈H₃₈O₂S [M + H]⁺: 799.2593, found 799.2669.

Synthesis of Nq[10]CPP

To a dried 5 mL Schlenk containing a magnetic stirring bar were added **oxTh[10]CPP** (19 mg, 0.02 mmol, 1.0 eq), 1,4-benzoquinone (26 mg, 0.2 mmol, 10.0 eq) and the flask was evacuated and filled with argon three times. Subsequently, phenyl ether (400 μL) was added via syringe. Then, the mixture was allowed to react at 200 °C for 2 days. After cooling to r.t, the reaction mixture was poured into hexane and the precipitate was collected. Dissolve the precipitate in dichloromethane. After purifying by column chromatography on silica gel (petroleum

ether/CH$_2$Cl$_2$ = 1/4, v/v) to get **Nq[10]CPP** as a red solid (Yield: 6.2 mg, 37 %). M.p. > 300 °C. ^{1}H NMR (600 MHz, CD$_2$Cl$_2$, 298 K) δ: 7.59–7.58 (m, 28H), 7.55 (d, J = 8.6 Hz, 4H), 7.29 (d, J = 8.6 Hz, 4H), 7.05 (s, 2H), 6.97 (s, 2H). ^{13}C NMR (150 MHz, CD$_2$Cl$_2$, 298 K) δ: 185.6, 142.1, 141.3, 139.1, 139.1, 138.8, 138.7, 138.6, 138.5, 138.5, 130.5, 129.6, 127.8, 127.8, 127.7, 127.7, 127.4. HR-MS (MALDI-TOF) calculated for C$_{64}$H$_{40}$O$_2$ M: 840.3028, found 840.3027.

Synthesis of Aq[10]CPP

To a dried 5 mL Schlenk containing a magnetic stirring bar were added **oxTh[10]CPP** (17 mg, 0.02 mmol, 1.0 eq), 1,4-Naphthoquinone (32 mg, 0.2 mmol, 10.0 eq) and the flask was evacuated and filled with argon three times. Subsequently, phenyl ether (400 μL) was added via syringe. Then, the mixture was allowed to react at 200 °C for 2 days. After cooling to r.t, the reaction mixture was poured into hexane, and the precipitate was collected. Dissolve the precipitate in dichloromethane. After purifying by column chromatography on silica gel (petroleum ether/CH$_2$Cl$_2$ = 1/4, v/v) to get **Aq[10]CPP** as an orange solid (Yield: 9.0 mg, 51 %). M.p. > 300 °C. ^{1}H NMR (600 MHz, CD$_2$Cl$_2$, 298 K) δ: 8.23-8.22 (m, 2H), 7.83-7.82 (m, 2H), 7.60–7.56 (m, 32H), 7.33 (d, J = 8.6 Hz, 4H), 7.11 (s, 2H). ^{13}C NMR (150 MHz, CD$_2$Cl$_2$, 298 K) δ 184.0, 142.9, 142.1, 138.9, 138.8, 138.8, 138.7, 138.6, 138.6, 138.5, 134.5, 134.3, 132.6, 129.5, 127.8, 127.8, 127.8, 127.7, 127.5, 127.3. HR-MS (MALDI-TOF) calculated for C$_{68}$H$_{42}$O$_2$ M: 890.3185, found 890.3173.

Synthesis of Tq[10]CPP

To a dried 5 mL Schlenk containing a magnetic stirring bar were added oxTh[10]CPP (11 mg, 0.01 mmol, 1.0 eq), 1,4-Anthraquinone (29 mg, 0.1 mmol, 10.0 eq) and the flask was evacuated and filled with argon three times. Subsequently, phenyl ether (300 μL) was added via syringe. Then, the mixture was allowed to react at 200 °C for 2 days. After cooling to r.t, the reaction mixture was poured into hexane and the precipitate was collected. Dissolve the precipitate in dichloromethane. After purifying by column chromatography on silica gel (petroleum ether/CH$_2$Cl$_2$ = 1/4, v/v) to get Tq[10]CPP as an orange solid (Yield: 4.0 mg, 43 %). M.p. > 300 °C. ^{1}H NMR (600 MHz, CD$_2$Cl$_2$, 298 K) δ: 8.77 (s, 2H), 8.15-8.14 (m, 2H), 7.74-7.72 (m, 2H), 7.60-7.56 (m, 32H), 7.36 (d, J = 8.7 Hz, 4H), 7.14 (s, 2H). ^{13}C NMR (150 MHz, CD$_2$Cl$_2$, 298 K) δ: 184.0, 143.0, 142.2, 138.9, 138.8, 138.6, 135.6, 133.8, 131.0, 130.4, 129.8, 129.4, 129.4, 127.8, 127.7, 127.5. HR-MS (MALDI-TOF) calculated for C$_{72}$H$_{44}$O$_2$ M: 940.3341, found 940.3332.

Data availability

The data generated in this study are available within the article, Supplementary Information, and Source Data. Source data is available for Figs. 4, 6, 8, 9, and Supplementary Figures S5-S9 in the associated source data file. The X-ray crystallographic coordinates for structures reported in this study have been deposited at the Cambridge Crystallographic Data Centre (CCDC), under deposition numbers CCDC 2253427 for **Th[10]CPP**, 2336673 for **Nq[10]CPP** and 2280928 for **Aq[10]CPP**. These data can be obtained free of charge from The Cambridge Crystallographic Data Centre via www.ccdc.cam.ac.uk/data_request/cif. All additional data are available from the corresponding author upon request. Source data are provided with this paper.

References

1. Jasti, R., Bhattacharjee, J., Neaton, J. B. & Bertozzi, C. R. Synthesis, characterization, and theory of [9]-, [12]-, and [18]cycloparaphenylene: carbon nanohoop structures. *J. Am. Chem. Soc.* **130**, 17646–17647 (2008).
2. Lewis, S. E. Cycloparaphenylenes and related nanohoops. *Chem. Soc. Rev.* **44**, 2221–2304 (2015).
3. Darzi, E. R. & Jasti, R. The dynamic, size-dependent properties of [5]-[12]cycloparaphenylenes. *Chem. Soc. Rev.* **44**, 6401–6410 (2015).
4. Leonhardt, E. J. & Jasti, R. Emerging applications of carbon nanohoops. *Nat. Rev. Chem.* **3**, 672–686 (2019).
5. Fan, Y., He, J., Guo, S. & Jiang, H. Host-Guest Chemistry in Binary and Ternary Complexes Utilizing π-Conjugated Carbon Nanorings. *ChemPlusChem* **89**, e202300536 (2024).
6. Fan, Y. et al. Chiral Carbon Nanorings: Synthesis, Properties and Hierarchical Self-assembly of Chiral Ternary Complexes Featuring a Narcissistic Chiral Self-Recognition for Chiral Amines. *Angew. Chem. Int. Ed.* **62**, e2023046 (2023).
7. Fan, Y.-Y. et al. An isolable catenane consisting of two Möbius conjugated nanohoops. *Nat. Commun.* **9**, 3037 (2018).
8. Xu, Y. et al. Concave-Convex pi-pi Template Approach Enables the Synthesis of [10]Cycloparaphenylene-Fullerene [2]Rotaxanes. *J. Am. Chem. Soc.* **140**, 13413–13420 (2018).
9. Segawa, Y. et al. Topological molecular nanocarbons: All-benzene catenane and trefoil knot. *Science* **365**, 272–276 (2019).
10. Van Raden, J. M., White, B. M., Zakharov, L. N. & Jasti, R. Nanohoop Rotaxanes from Active Metal Template Syntheses and Their Potential in Sensing Applications. *Angew. Chem. Int. Ed.* **58**, 7341–7345 (2019).
11. Segawa, Y., Kuwayama, M. & Itami, K. Synthesis and Structure of [9] Cycloparaphenylene Catenane: An All-Benzene Catenane Consisting of Small Rings. *Org. Lett.* **22**, 1067–1070 (2020).
12. Van Raden, J. M., Jarenwattananon, N. N., Zakharov, L. N. & Jasti, R. Active Metal Template Synthesis and Characterization of a Nanohoop [c2]Daisy Chain Rotaxane. *Chem. Eur. J.* **26**, 10205–10209 (2020).
13. Bu, A. et al. A Conjugated Covalent Template Strategy for All-Benzene Catenane Synthesis. *Angew. Chem. Int. Ed.* **61**, e202209449 (2022).
14. Patrick, C. W. et al. Polyyne [3]Rotaxanes: Synthesis via Dicobalt Carbonyl Complexes and Enhanced Stability. *Angew. Chem. Int. Ed.* **61**, e202116897 (2022).
15. May, J. H., Van Raden, J. M., Maust, R. L., Zakharov, L. N. & Jasti, R. Active template strategy for the preparation of π-conjugated interlocked nanocarbons. *Nat. Chem.* **15**, 170–176 (2023).
16. Steudel, F. M. et al. Synthesis of C$_{60}$/[10]CPP-Catenanes by Regioselective, Nanocapsule-Templated Bingel Bis-Addition. *Angew. Chem. Int. Ed.* **62**, e202309393 (2023).
17. Ishibashi, H. et al. Noncovalent Modification of Cycloparaphenylene by Catenane Formation Using an Active Metal Template Strategy**. *Angew. Chem. Int. Ed* **62**, e202310613 (2023).
18. May, J. H., Fehr, J. M., Lorenz, J. C., Zakharov, L. N. & Jasti, R. A High-Yielding Active Template Click Reaction (AT-CuAAC) for the Synthesis of Mechanically Interlocked Nanohoops. *Angew. Chem. Int. Ed.* **63**, e202401823 (2024).
19. Lu, D. et al. The Supramolecular Chemistry of Cycloparaphenylenes and Their Analogs. *Front. Chem.* **7**, 668 (2019).
20. Ubasart, E. et al. A three-shell supramolecular complex enables the symmetry-mismatched chemo- and regioselective bis-functionalization of C$_{60}$. *Nat. Chem.* **13**, 420–427 (2021).
21. Guo, S. et al. Monitoring Hierarchical Assembly of Ring-in-Ring and Russian Doll Complexes Based on Carbon Nanoring by Förster Resonance Energy Transfer. *JACS Au* **4**, 402–410 (2024).
22. Kayahara, E. et al. Gram-Scale Syntheses and Conductivities of [10] Cycloparaphenylene and Its Tetraalkoxy Derivatives. *J. Am. Chem. Soc.* **139**, 18480–18483 (2017).
23. Pérez-Guardiola, A., Pérez-Jiménez, Á. J., Muccioli, L. & Sancho-García, J. C. Structure and Charge Transport Properties of Cycloparaphenylene Monolayers on Graphite. *Adv. Mater. Interfaces* **6**, 1801948 (2019).
24. Lucas, F. et al. [4]Cyclo-N-ethyl-2,7-carbazole: Synthesis, Structural, Electronic and Charge Transport Properties. *Chem. Eur. J.* **25**, 7740–7748 (2019).

25. Mun, J. et al. Conjugated Carbon Cyclic Nanorings as Additives for Intrinsically Stretchable Semiconducting Polymers. *Adv. Mater.* **31**, 1903912 (2019).

26. Lucas, F. et al. [4]Cyclo-N-alkyl-2,7-carbazoles: Influence of the Alkyl Chain Length on the Structural, Electronic, and Charge Transport Properties. *J. Am. Chem. Soc.* **143**, 8804–8820 (2021).

27. Lv, Y. et al. Single cycloparaphenylene molecule devices: Achieving large conductance modulation via tuning radial π-conjugation. *Sci. Adv.* **7**, eabk3095 (2021).

28. Wang, S. et al. Du, P., Facile Synthesis of a Conjugated Macrocyclic Nanoring with Graphenic Hexabenzocoronene Sidewall as the Segment of [12,12] Carbon Nanotubes. *Eur. J. Org. Chem.* **2022**, e202101493 (2022).

29. Chen, D. et al. A Donor–Acceptor 10-Cycloparaphenylene and Its Use as an Emitter in an Organic Light-Emitting Diode. *Org. Lett.* **25**, 998–1002 (2023).

30. Brouillac, C. et al. [4]-Cyclo-2,7-Carbazole as Host Material in High-Efficiency Phosphorescent OLEDs: A New Perspective for Nanohoops in Organic Electronics. *Adv. Opt. Mater.* **11**, 2202191 (2023).

31. Lucas, F. et al. Electronic and Charge Transport Properties in Bridged versus Unbridged Nanohoops: Role of the Nanohoop Size. *Chem. Eur. J.* **29**, e202300934 (2023).

32. Roy, R., Brouillac, C., Jacques, E., Quinton, C. & Poriel, C. π-Conjugated Nanohoops: A New Generation of Curved Materials for Organic Electronics. *Angew. Chem. Int. Ed.* **63**, e202402608 (2024).

33. White, B. M. et al. Expanding the Chemical Space of Biocompatible Fluorophores: Nanohoops in Cells. *ACS Cent. Sci.* **4**, 1173–1178 (2018).

34. Qiu, Z. L. et al. Well-Defined Segment of Carbon Nanotube with Bright Red Emission for Three-Photon Fluorescence Cerebrovascular Imaging. *Adv. Opt. Mater.* **9**, 2100482 (2021).

35. Sato, K. et al. Circularly Polarized Luminescence of a Stereogenic Curved Paraphenylene Anchoring a Chiral Binaphthyl in Solution and Solid State. *Chem. Eur. J.* **27**, 1323–1329 (2020).

36. He, J. et al. Nanosized Carbon Macrocycles Based on a Planar Chiral Pseudo Meta-[2.2]Paracyclophane. *Chem. Eur. J.* **28**, e202103832 (2022).

37. Fang, P., Chen, M., Zhang, X. & Du, P. Selective synthesis and (chir) optical properties of binaphthyl-based chiral carbon macrocycles. *Chem. Commun.* **58**, 8278–8281 (2022).

38. He, J. et al. Lemniscular carbon nanohoops with contiguous conjugation from planar chiral [2.2]paracyclophane: influence of the regioselective synthesis on topological chirality. *Chem. Sci.* **14**, 4426–4433 (2023).

39. Xu, Y. et al. [n]Cycloparaphenylene-Pillar[5]arene Bismacrocycles: Their Circularly Polarized Luminescence and Multiple Guest Recognition Properties. *Angew. Chem. Int. Ed.* **62**, e202302978 (2023).

40. Guo, S. et al. Highly Luminescent Chiral Carbon Nanohoops via Symmetry Breaking with a Triptycene Unit: Bright Circularly Polarized Luminescence and Size-Dependent Properties. *Small* **20**, 2308429 (2024).

41. Wu, D., Cheng, W., Ban, X. & Xia, J. Cycloparaphenylenes (CPPs): An Overview of Synthesis, Properties, and Potential Applications. *J. Org. Chem.* **7**, 2161–2181 (2018).

42. Xu, Y. & von Delius, M. The Supramolecular Chemistry of Strained Carbon Nanohoops. *Angew. Chem. Int. Ed.* **59**, 559–573 (2019).

43. Wang, J., Zhang, X., Jia, H., Wang, S. & Du, P. Large π-Extended and Curved Carbon Nanorings as Carbon Nanotube Segments. *Acc. Chem. Res* **54**, 4178–4190 (2021).

44. Ari, D. et al. Modulation of [8]CPP properties by bridging two phenylene units. *Chem. Commun.* **59**, 14835–14838 (2023).

45. Zhang, R., An, D., Zhu, J., Lu, X. & Liu, Y. Carbon Nanorings and Nanobelts: Material Syntheses, Molecular Architectures, and Applications. *Adv. Funct. Mater.* **33**, 2305249 (2023).

46. Shen, Y.-J., Zhu, K.-L., Liang, J.-Q., Sun, X. & Gong, H.-Y. Carbon-rich macrocycles and carbon nanoribbons as unique optical materials. *J. Mater. Chem. C.* **11**, 4267–4287 (2023).

47. Fan, Y. et al. Efficient manipulation of Forster resonance energy transfer through host-guest interaction enables tunable white-light emission and devices in heterotopic bisnanohoops. *Chem. Sci.* **14**, 11121–11130 (2023).

48. Li, X. et al. A nonalternant azulene-embedded carbon nanohoop featuring anti-Kasha emission and tunable properties upon pH stimuli-responsiveness. *J. Mater. Chem. C.* **11**, 1429–1434 (2023).

49. Guo, S. et al. Naphthalene Diimide-Embedded Donor-Acceptor Carbon Nanohoops: Photophysical, Photoconductive and Charge Transport Properties. *ACS Applied Materials & Interfaces.* am-2024-193496, accept (2025).

50. Yang, H. et al. Neutral and Dicationic [5]helicene-embedded Cycloparaphenylene Nanohoops with Möbius Topology and Local/In-Plane Aromaticity. *ChemRxiv.* https://doi.org/10.26434/chemrxiv-2024-vxf63-v2 (2024).

51. Lovell, T. C., Fosnacht, K. G., Colwell, C. E. & Jasti, R. Effect of curvature and placement of donor and acceptor units in cycloparaphenylenes: a computational study. *Chem. Sci.* **11**, 12029–12035 (2020).

52. Hoheisel, T. N., Schrettl, S., Szilluweit, R. & Frauenrath, H. Nanostructured Carbonaceous Materials from Molecular Precursors. *Angew. Chem. Int. Ed.* **49**, 6496–6515 (2010).

53. Bunz, U. H., Menning, S. & Martin, N. para-Connected cyclophenylenes and hemispherical polyarenes: building blocks for single-walled carbon nanotubes? *Angew. Chem. Int. Ed.* **51**, 7094–7101 (2012).

54. Hermann, M., Wassy, D. & Esser, B. Conjugated Nanohoops Incorporating Donor, Acceptor, Hetero- or Polycyclic Aromatics. *Angew. Chem. Int. Ed.* **60**, 15743–15766 (2021).

55. Rasul, R. et al. Alkali metals doped cycloparaphenylene nanohoops: Promising nonlinear optical materials with enhanced performance. *Heliyon* **9**, e21508 (2023).

56. Yamago, S., Kayahara, E. & Iwamoto, T. Organoplatinum-Mediated Synthesis of Cyclic π-Conjugated Molecules: Towards a New Era of Three-Dimensional Aromatic Compounds. *Chem. Rec.* **14**, 84–100 (2014).

57. Kuwabara, T., Orii, J., Segawa, Y. & Itami, K. Curved Oligophenylenes as Donors in Shape-Persistent Donor-Acceptor Macrocycles with Solvatofluorochromic Properties. *Angew. Chem.* **127**, 9782–9785 (2015).

58. Darzi, E. R. et al. Synthesis, Properties, and Design Principles of Donor-Acceptor Nanohoops. *ACS Cent. Sci.* **1**, 335–342 (2015).

59. Lovell, T. C., Garrison, Z. R. & Jasti, R. Synthesis, Characterization, and Computational Investigation of Bright Orange-Emitting Benzothiadiazole [10. Cycloparaphenylene. *Angew. Chem. Int.* **59**, 14363–14367 (2020).

60. Qiu, Z. L. et al. Tetra-benzothiadiazole-based [12]Cycloparaphenylene with Bright Emission and Its Supramolecular Assembly. *Angew. Chem. Int. Ed.* **59**, 20868–20872 (2020).

61. Deng, H. et al. Modular synthesis, host–guest complexation and solvation-controlled relaxation of nanohoops with donor–acceptor structures. *Chem. Sci.* **13**, 14080–14089 (2022).

62. Schwer, F. et al. Synthesis and C_{60} Binding of Aza[10]CPP and N-Methylaza[10]CPP. *Org. Mater.* **4**, 7–17 (2022).

63. Bliksted Roug Pedersen, V. et al. Synthesis and Properties of Fluorenone-Containing Cycloparaphenylenes and Their Late-Stage Transformation. *Chem. Eur. J.* **30**, e202303490 (2024).

64. Wang, F. & Liu, X. Multicolor tuning of lanthanide-doped nanoparticles by single wavelength excitation. *Acc. Chem. Res.* **47**, 1378–1385 (2014).

65. Wang, S. & Wang, L. Lanthanide-doped nanomaterials for luminescence detection and imaging. *Trends Anal. Chem.* **62**, 123–134 (2014).

66. Li, H., Wang, X., Huang, D. & Chen, G. Recent advances of lanthanide-doped upconversion nanoparticles for biological applications. *Nanotechnology* **31**, 072001 (2020).

67. Chen, Z., Ho, C. L., Wang, L. & Wong, W. Y. Single-Molecular White-Light Emitters and Their Potential WOLED Applications. *Adv. Mater.* **32**, 1903269 (2020).

68. Zhang, J. et al. White-light emission from organic aggregates: a review. *Adv. Photonics* **4**, 014001 (2021).

69. Gan, N., Zou, X., Zhang, Y., Gu, L. & An, Z. Recent advances in multicolor organic room-temperature phosphorescence. *Appl. Phys. Rev.* **10**, 021313 (2023).

70. Zhang, Y. et al. Multicolor Afterglow Carbon Dots: Luminescence Regulation, Preparation, and Application. *Adv. Funct. Mater.* **34**, 2315366 (2024).

71. Zhang, Y. et al. Single-Molecule-based White-Light Emissive Organic Solids with Molecular-Packing-Dependent Thermally Activated Delayed Fluorescence. *J. Phys. Chem. Lett.* **8**, 4808–4813 (2017).

72. Zhou, C. et al. Ternary Emission of Fluorescence and Dual Phosphorescence at Room Temperature: A Single-Molecule White Light Emitter Based on Pure Organic Aza-Aromatic Material. *Adv. Funct. Mater.* **28**, 1802407 (2018).

73. Li, Q. et al. Pillararene-Induced Intramolecular Through-Space Charge Transfer and Single-Molecule White-Light Emission. *Angew. Chem. Int. Ed.* **61**, e202202381 (2022).

74. Tu, D. et al. Highly Emissive Organic Single-Molecule White Emitters by Engineering o-Carborane-Based Luminophores. *Angew. Chem. Int. Ed.* **56**, 11370–11374 (2017).

75. Li, C. et al. An Organic Emitter Displaying Dual Emissions and Efficient Delayed Fluorescence White OLEDs. *Adv. Opt. Mater.* **7**, 1801667 (2019).

76. Shao, S., Ding, J., Wang, L., Jing, X. & Wang, F. White electroluminescence from all-phosphorescent single polymers on a fluorinated poly(arylene ether phosphine oxide) backbone simultaneously grafted with blue and yellow phosphors. *J. Am. Chem. Soc.* **134**, 20290–20293 (2012).

77. Mao, Z. et al. Linearly tunable emission colors obtained from a fluorescent-phosphorescent dual-emission compound by mechanical stimuli. *Angew. Chem. Int. Ed.* **54**, 6270–6273 (2015).

78. He, Z. et al. White light emission from a single organic molecule with dual phosphorescence at room temperature. *Nat. Commun.* **8**, 416 (2017).

79. Yang, Q. Y. & Lehn, J. M. Bright white-light emission from a single organic compound in the solid state. *Angew. Chem. Int. Ed.* **53**, 4572–4577 (2014).

80. Chen, Y. H. et al. Insight into the mechanism and outcoupling enhancement of excimer-associated white light generation. *Chem. Sci.* **7**, 3556–3563 (2016).

81. Nakayama, J., Yamaoka, S., Nakanishi, T. & Hoshino, M. 3,4-Di-tert-butylthiophene 1,1-dioxide, a convenient precursor of o-Di-tert-butylbenzene and its derivatives. *J. Am. Chem. Soc.* **110**, 6598–6599 (1988).

82. Dmowski, W., Manko, V. A. & Nowak, I. 3-Chloro-4-fluorothiophene-1,1-dioxide. A new synthetically useful fluorodiene. *J. Fluor. Chem.* **88**, 143–151 (1998).

83. Gentry, J. W. The legacy of John Tyndall in aerosol science. *J. Aerosol Sci.* **28**, 1365–1372 (1997).

Author contributions

H.J. proposed the concept. X.L. designed the experiments, synthesized the compounds, carried out the characterizations, collected and analyzed the data. Z.L., J.H. and S.G. participated in partial experiments. L.L., L.J., Y.W. and X.C. carried out theory calculations. H.J. and X.L. wrote the manuscript. H.J. supervised the project and revised the manuscript. All authors participated in the discussion and revised the manuscript.

Competing interests

The authors declare no competing interests.

Additional information

Supplementary information The online version contains supplementary material available at https://doi.org/10.1038/s41467-025-55895-x.

Correspondence and requests for materials should be addressed to Ying Wang, Xuebo Chen or Hua Jiang.

Peer review information *Nature Communications* thanks the anonymous reviewer(s) for their contribution to the peer review of this work. A peer review file is available.

Reprints and permissions information is available at http://www.nature.com/reprints

Publisher's note Springer Nature remains neutral with regard to jurisdictional claims in published maps and institutional affiliations.